

Article

Visible Light-Responsive Sulfone-Based Covalent Organic Framework as Metal-Free Nanoenzyme for Visual Colorimetric Determination of Uranium

Yulong Xu, Jiahui Wei and Xuwei Chen * 

College of Sciences, Northeastern University, Shenyang 110819, China; 1910030@stu.neu.edu.cn (Y.X.); 1910051@stu.neu.edu.cn (J.W.)

* Correspondence: chenxuwei@mail.neu.edu.cn

Abstract: Covalent organic framework (COF) has been attracting considerable attention as a novel crystalline material owing to its extended π -electron conjugation and excellent spectral behavior. In this study, we present an imine-linked two-dimensional (2D) crystalline sulfone-based covalent organic framework (TAS-COF) synthesized by 2,4,6-triformylphloroglucinol (Tp) and 3,7-diaminodibenzo[b,d]thiophene (DAS) via a Schiff base condensation reaction. The benzothio-phenone sulfone endows the as-synthesized TAS-COF with excellent oxidase-like activity under visible light irradiation, ascribed to the generation of superoxide radicals ($O_2^{\bullet-}$) by photo-generated electron transfer. TAS-COF can efficiently oxidase the colorless substrate 3,3',5,5'-tetramethylbenzidine (TMB) into blue oxidized TMB (oxTMB) when exposed to visible light, and the presence of uranium (UO_2^{2+}) leads to clear color fading due to the coordination between the imine of oxTMB and UO_2^{2+} . A colorimetric strategy is thus developed for UO_2^{2+} determination with a detection limit of $0.07 \mu\text{mol L}^{-1}$. Moreover, a paper-based visual sensing platform is also constructed to offer simple and fast UO_2^{2+} content evaluation in water samples. The present study not only provides a promising strategy to prepare visible light-triggered COF-based metal-free nanoenzymes but also extends the applications of COF material in radionuclide detection.

Keywords: covalent organic framework; oxidase-like activity; colorimetry; uranium; visible light



Citation: Xu, Y.; Wei, J.; Chen, X. Visible Light-Responsive Sulfone-Based Covalent Organic Framework as Metal-Free Nanoenzyme for Visual Colorimetric Determination of Uranium. *Chemosensors* **2022**, *10*, 248. <https://doi.org/10.3390/chemosensors10070248>

Academic Editors: Zhuangqiang Gao, Philip Gardiner and Luis Crovetto

Received: 6 June 2022

Accepted: 26 June 2022

Published: 28 June 2022

Publisher's Note: MDPI stays neutral with regard to jurisdictional claims in published maps and institutional affiliations.



Copyright: © 2022 by the authors. Licensee MDPI, Basel, Switzerland. This article is an open access article distributed under the terms and conditions of the Creative Commons Attribution (CC BY) license (<https://creativecommons.org/licenses/by/4.0/>).

1. Introduction

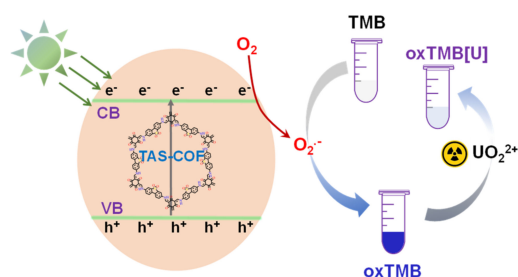
It is of great importance to utilize renewable resources urgently for sustainable development, and the high density of nuclear power and its low emission of greenhouse gases have made the issue extremely attractive [1]. In the nuclear industry, UO_2^{2+} is the most widely used fuel to generate nuclear power and even if is beneficial for sustainable development [2], there has been concern about uranium leaching due to the massive mining and processing of uranium, improper handling of nuclear waste, and undesirable nuclear accidents in recent years [3]. UO_2^{2+} can reside in the environment for a long time due to its stability, posing a serious risk to human and animal health, such as cancer and irreversible renal injury [4,5]. Among the methodologies for monitoring the UO_2^{2+} level in the environment, the conventional techniques such as inductively coupled plasma mass spectrometry (ICP-MS) [6], Raman spectroscopy [7], and atomic absorption spectroscopy (AAS) [8] have been demonstrated to be quite powerful in achieving sensitive determination. However, the expensive instrumentation, tedious sample preparation process, and the requirement of professional manipulation restrict their application in quick field investigations. At this point, colorimetry has become a preferred tool owing to its ease of operation, rapid observation with the naked eye, favorable sensitivity, and attractive flexibility. Lu et al., reported the colorimetric determination of UO_2^{2+} by DNAzyme-modified gold nanoparticles (AuNPs) with excellent selectivity and high sensitivity, based on the uranyl induced disassembly of AuNP aggregates [9]. Liu et al., designed a visual colorimetric of a UO_2^{2+}

detection protocol using *o*-phosphoryl ethanolamine-functionalized gold nanoparticles as the spectral probe, based on the ability of UO_2^{2+} to induce the aggregation of AuNPs [10]. He et al., found that UO_2^{2+} showed specific artificial peroxidase activity towards substrate 2,2'-azino-bis(3-ethylbenzothiazoline-6-sulfonic acid) diammonium (ABTS) and proposed a facile and reliable colorimetric protocol for UO_2^{2+} assay with a detection limit of 0.5 μM [11]. Though these colorimetric processes provide favorable sensitivity for UO_2^{2+} monitoring, they are usually troubled by complex labeling processes or surface functionalization procedures, and the instability of the spectral probes.

To date, numerous nanomaterials have been explored with favorable mimic enzyme activity, such as Q-graphene [12], V_2O_5 nanobelts [13], metal-organic frameworks [14], noble metal nanoparticles [15], and alloy nanoparticles [16]. By virtue of their high stability, low cost, facial synthesis, and tunable catalytic activity, these inorganic nanomaterial-based artificial enzymes can effectively avoid the inherent limitations of natural enzymes and have been widely used in the field of biomedicine and sensing. Most of the reported nanoenzymes are made of nanoscale metals, metal oxides, or metal-based frameworks, and few metal-free nanozymes are reported except for some carbon-based nanomaterials (graphene, carbon dots) and amorphous polymers with poor stability and limited enzyme activities [17–19].

Covalent organic frameworks (COFs) are emerging porous crystalline polymers linked via covalent bonding and merited with excellent stability, tunable functionality, low skeleton density, and regular periodic pore structures. Some COF materials show attractive light-responsive prosperities relying on their π - π array framework and high crystallinity [20]. Qiu et al., found that the two-dimensional COF (Tph-BDP) prepared by 5,10,15,20-tetrakis(4-aminophenyl)-21*H*,23*H*-porphyrin and 5,5-difluoro-2,8-diformyl-1,3,7,9-tetramethyl-10-phenyl-5*H*-dipyrrolo [1,2-*c*:2',1'-*f*][1,3,2]diazaborin-4-ium-5-uide exhibited favorable simulated oxidase activity under 635 nm laser irradiation, due to its low energy level bandgap [21]. Chen and co-workers reported the preparation of a three-dimensional COF (COF-300-AR) by terephthalaldehyde and tetrakis (4-aminophenyl) methane. COF-300-AR has shown excellent oxidase-mimicking activity under purple light stimulation and has been successfully applied in the sensitive detection of glutathione (GSH) [22].

Herein, a visible light-responsive sulfone-based COF (TAS-COF) was fabricated with electron-rich aromatic C_3 -symmetric 2,4,6-triformylphloroglucinol and sulfone substituted phenyl edges of C_2 -symmetric 3,7-diaminodibenzo[*b,d*]thiophene sulfone as the building blocks via a Schiff base condensation reaction. It is interesting to note that the TAS-COF exhibited favorable oxidase-like activity under visible light irradiation, which could oxidize the colorless 3,3',5,5'-tetramethylbenzidine into blue oxTMB when exposed under a white-light LED. Due to the ability of UO_2^{2+} to coordinate with the imines of oxTMB, the addition of UO_2^{2+} induces clear color fading of the sensing system. As illustrated in Scheme 1, a colorimetric sensing platform was thus constructed for the sensitive and selective detection of UO_2^{2+} content based on the visible light-triggered oxidase-like activity of TAS-COF. In addition, a paper-based detection platform is also constructed by visual monitoring of the color variations with targeted UO_2^{2+} at different concentrations, demonstrating the great potential of this sensing system in on-the-spot evaluation of UO_2^{2+} content in real water samples.



Scheme 1. Illustration for colorimetric detection of UO_2^{2+} with visible light-responsive TAS-COF.

2. Materials and Methods

2.1. Materials

2,4,6-triformylphloroglucinol (Tp) and 3,7-diaminodibenzo[b,d]thiophene sulfone (DAS) were purchased from Bide Pharmatech Ltd. (Shanghai, China). Acetone, tetrahydrofuran (THF), *o*-dichlorobenzene (*o*-DCB), *n*-butanol (*n*-BuOH), acetic acid (HAC), sodium acetate, 3,3',5,5'-tetramethylbenzidine (TMB), *o*-Phenylenediamine (OPD), and other reagents were purchased from Aladdin Industrial Inc. (Shanghai, China). Ultrapure water was prepared from the Millipore system. All reagents were analytical grade and used without further purification.

Ultraviolet-visible (UV-vis) absorption spectra were obtained on a U-3900 UV-vis spectrophotometer (Hitachi, Tokyo, Japan). Powder X-ray diffraction (PXRD) patterns were collected on a Maxima XRD-7000 diffractometer (Shimadzu, Kyoto, Japan). Scanning electron microscopy (SEM) images were collected on a SU8010 field-emission electron microscope at a voltage of 5.0 kV (Hitachi, Tokyo, Japan). Fourier transform infrared (FT-IR) spectra were recorded using a Nicolet-6700 FT-IR spectrophotometer (Thermo Scientific, Massachusetts State, USA). The concentrations of UO_2^{2+} in practical samples were determined using an iCAP Q inductively coupled plasma mass spectrometer (ICP-MS, Thermo Fisher Scientific, USA). Visible light was generated by a white-light LED lamp ($\lambda \geq 420$ nm, power density $62 \text{ mW} \cdot \text{cm}^{-2}$, Guanyu Lighting Co., Ltd., Guangzhou, China).

2.2. Synthesis of TAS-COF

A 10-mL Pyrex tube was charged with Tp (16.8 mg, 0.08 mmol), DAS (29.6 mg, 0.12 mmol), *o*-DCB (1 mL), *n*-BuOH (1 mL), and HAC (6 mol L^{-1} , 0.2 mL). This mixture was homogenized under sonication for 10 min and degassed by three freeze-pump-thaw cycles. Then the Pyrex tube was sealed off and heated at 120 °C for 72 h. The precipitate was collected via centrifugation and washed with 10 mL anhydrous THF and 10 mL acetone, in turn, three times at room temperature. The obtained powder was dried at 80 °C under vacuum for 12 h, giving the product of TAS-COF a yield of 83%

2.3. Steady-State Kinetic Studies of TAS-COF as Oxidase Mimic

The steady-state kinetic studies were performed in 300 μL reaction buffer (0.2 mol L^{-1} HAC-NaAc, pH 3.5) comprising 0.2 mg mL^{-1} TAS-COF and varied concentrations of TMB under irradiation by a white-light LED lamp ($\lambda \geq 420$ nm) for 10 min. All reactions were carried out three times and the related spectra were recorded. The rate of enzymatic catalytic reaction was described by the following Michaelis–Menten equation [23]:

$$V = V_{\max}[S] / (K_m + [S])$$

where V and V_{\max} were the relating reaction rate, and the maximum rate achieved by the system. $[S]$ was TMB concentration. K_m was the Michaelis–Menten constant.

2.4. Colorimetric Detection of UO_2^{2+}

Typically, 100 μL TAS-COF solution (0.2 mg mL^{-1}) was mixed with HAC-NaAc buffer (200 μL , pH 3.5) at room temperature, then 100 μL TMB solution (0.5 mmol L^{-1}) and 100 μL UO_2^{2+} solution were added sequentially. The resultant mixture was exposed to a white-light LED lamp ($\lambda \geq 420$ nm, 63 mW cm^{-2}) to trigger the catalysis activity of TAS-COF. After irradiation for 10 min, the absorbance of this system at 650 nm (A) was recorded. The blank signal of the sensing system (A_0) was achieved without the addition of UO_2^{2+} , and the absorbance difference ($A_0 - A$) was exploited for the fabrication of the calibration curve.

For selectivity investigations, 100 μL of different potential interferents (10 mmol L^{-1}) including Na^+ , K^+ , Mn^{2+} , Cu^{2+} , Ni^{2+} , Ca^{2+} , Mg^{2+} , Pb^{2+} , Cd^{2+} , Zn^{2+} , and Cr^{3+} instead of UO_2^{2+} were added into the sensing system, and the spectral signal was recorded accordingly.

2.5. Analysis of UO_2^{2+} Content in Real Samples

Lake water samples collected from Nanhu (Shenyang, China) were centrifuged (8000 r min^{-1} , 10 min) and filtered with $0.22 \mu\text{m}$ membranes to remove large particles. Tap water samples were acquired from the laboratory. The UO_2^{2+} content in the water samples was monitored following the procedure depicted above.

2.6. Visual Inspection

Typically, $20 \mu\text{L}$ of 50 mg L^{-1} TAS-COF (prepared in 0.2 mol L^{-1} HAc-NaAc buffer) was dropped on a paper strip. An amount of $10 \mu\text{L}$ of TMB solution (30 mmol L^{-1}) and $10 \mu\text{L}$ UO_2^{2+} of different concentrations (0.5 mmol L^{-1} – 10 mmol L^{-1}) were sequentially added to the above point where the TAS-COF was located. The paper strip was then exposed to visible light irradiation from a LED for 10 min, and the color changes were recorded.

3. Results

3.1. Synthesis and Characterization of TAS-COF

The TAS-COF was synthesized with electron-rich aromatic C_3 -symmetric Tp and sulfone substituted phenyl edges of C_2 -symmetric DAS as the building blocks via a Schiff base condensation reaction and underwent irreversible keto-enol tautomerism (Figure 1A). The as-synthesized TAS-COF formed flower-like nanosheets (Figure 1B). As shown in Figure 1C, the EDS analysis results indicated that there were C, N, O, and S elements present in the TAS-COF material, and the elements were evenly distributed.

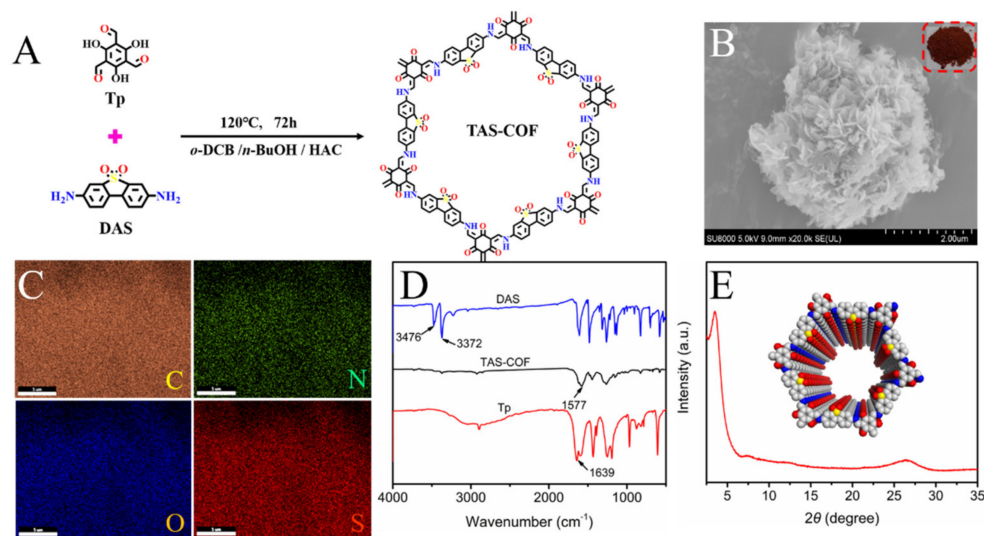


Figure 1. (A) Schematic representation for the preparation of TAS-COF. (B) SEM image of TAS-COF (Insert: the picture of TAS-COF). (C) EDS mapping of TAS-COF. (D) FT-IR spectra of Tp, DAS, and TAS-COF. (E) XRD pattern of TAS-COF (Insert: image of the space-filling diagram, gray: C, blue: N, red: O, yellow: S).

Figure 1D shows the FT-IR spectrum of the TAS-COF material. The bands centered at $\sim 3476 \text{ cm}^{-1}$ and $\sim 3372 \text{ cm}^{-1}$ were attributed to the asymmetrical and symmetrical stretching vibrations of aromatic amines of DAS, respectively. The peak at $\sim 1639 \text{ cm}^{-1}$ was allocated to the asymmetrical stretching vibrations of $-\text{C}=\text{O}$ of Tp. The new band at $\sim 1577 \text{ cm}^{-1}$ that appeared in the TAS-COF material was the characteristic peak of $-\text{C}=\text{N}$ stretching vibrations, suggesting the occurrence of a Schiff base condensation reaction between the monomers and the formation of an imine bond in the final COF product. The crystallinity of TAS-COF was then determined by powder X-ray diffraction (PXRD) and shown in Figure 1E. A set of intensive peaks at $2\theta = 3.46^\circ$ and 7.29° were observed in the PXRD pattern of TAS-COF, indicating that the obtained TAS-COF presents good crystallinity. Meanwhile,

the as-synthesized TAS-COF adopted an AA stacking mode with an interlayer distance of 3.70 Å, and the weak π - π stacking between the vertically stacked layers contributed to the appearance of a diffraction peak at $2\theta = 26^\circ$ [24]. The AA stacking mode provides a 1D channel, which was beneficial for quick electron transfer [25]. The above results indicated the successful preparation of the TAS-COF material with favorable crystallinity.

3.2. Visible Light Stimulated Oxidase-Like Activity of TAS-COF

To evaluate the oxidase-like activity of TAS-COF, three typical chromogenic substrates TMB, APTS, or OPD prepared in HAC-NaAc buffer (0.2 mol L^{-1}) were mixed with TAS-COF (0.2 mg mL^{-1}) and exposed to the irradiation from a white-light LED lamp. As shown in Figure 2A, after 10 min irradiation, obvious color changes (blue for TMB, green for APTS, yellow for OPD) were observed for the substrates, and the absorption maxima were 650 nm, 410 nm, and 445 nm, respectively, corresponding to the characteristic absorption of oxTMB, oxAPTS, and oxOPD, respectively. These suggest the excellent oxidase-like activity of TAS-COF under visible light irradiation, and the ability of TAS-COF to catalyze the oxidation of the above colorless substrates under visible light stimulation. Figure 2B depicts the band alignment of TAS-COF. The DFT calculation results indicate that the LUMO position of TAS-COF ($-1.32 \text{ V vs. Ag/AgCl}$) was lower than the oxygen's reduction potential ($-0.33 \text{ V vs. Ag/AgCl}$), indicating that the electrons in the LUMO of TAS-COF could theoretically reduce O_2 to generate $\text{O}_2^{\cdot-}$ [26]. Meanwhile, the absence of oxygen (N_2 -saturated experiment) caused a significant absorbance signal decrease in oxTMB (Figure 2C), suggesting oxygen dissolved in the water played an important role in the process of oxidation [27]. In order to prove this presumption, electron paramagnetic resonance (EPR) spectroscopy was conducted with 5,5-dimethyl-1-pyrroline-oxide (DMPO) as the $\text{O}_2^{\cdot-}$ radical trapping agent. As depicted in Figure 2D, TAS-COF exhibited a significantly $\text{O}_2^{\cdot-}$ signal under the while-light LED lamp irradiation. Meanwhile, the oxidase-like activity of TAS-COF to TMB presented a staircase-like behavior with the successive “on-off” of light irradiation, demonstrating its light-triggered catalytic activity (Figure 2E).

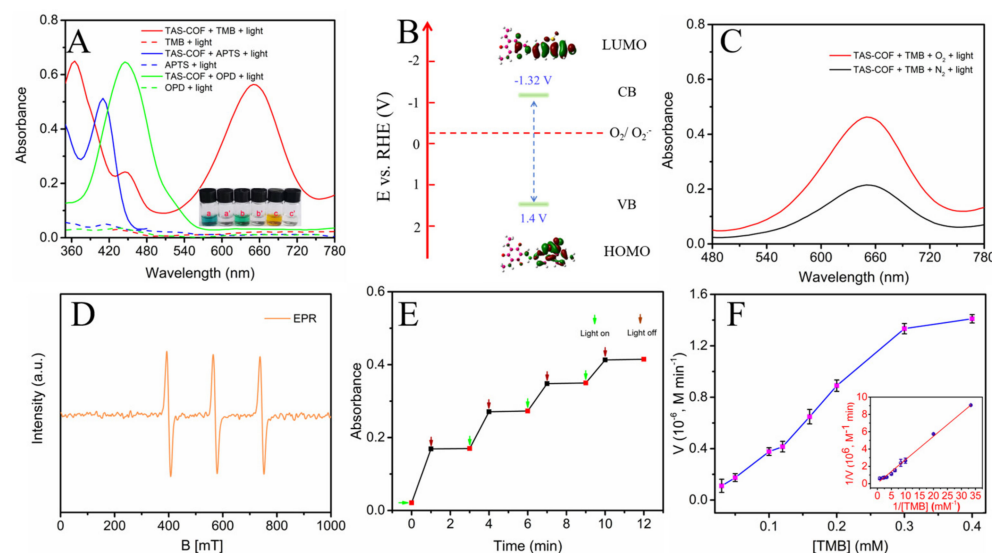


Figure 2. (A) UV-vis spectra of the system containing TMB, APTS, and OPD with/without TAS-COF in HAC-NaAc buffer (0.2 mol L^{-1}) under visible light irradiation. Insert: the images of the system containing TMB (a, a'), APTS (b, b'), and OPD (c, c') (B) Band alignment of TAS-COF (Insert: the images of LUMO and HOMO). (C) UV-vis spectrum of TAS-COF + TMB + O_2 and TAS-COF + TMB + N_2 under visible light irradiation. (D) EPR spectra of TAS-COF after illumination using white-light LED lamp for 10 min. (E) Staircase-like response of the oxidase-mimicking activity to light irradiation. (F) Steady-state kinetic assays of TAS-COF by varying TMB concentrations. Inset: Lineweaver–Burk plots of the catalytic capacity of TAS-COF with TMB as the substrate. The error bars represent the standard deviation ($n = 3$).

The steady-state kinetics of TAS-COF was then investigated to evaluate their catalytic activity and affinity to the substrate TMB. As illustrated in Figure 2F, the absorbance increased gradually with the TMB concentration. Based on the relationship between the corresponding initial reaction rates and the TMB concentration, the Lineweaver–Burk plot was obtained in Figure 2F. According to Michaelis–Menten equation [28], the Michaelis–Menten constant (K_m) and the maximum initial velocity (V_{max}) of TAS-COF were calculated to be 4.88 μM and $1.8 \times 10^{-4} \text{ M min}^{-1}$, respectively. Compared with the natural enzyme horseradish peroxidase (HRP) ($K_m = 0.434 \text{ mM}$, $V_{max} = 6 \times 10^{-6} \text{ M min}^{-1}$), TAS-COF showed a lower K_m and a higher V_{max} value, suggesting that TAS-COF as a metal-free nanoenzyme possessed superior affinity toward TMB and faster reaction rate [29].

3.3. Parameters Optimization for UO_2^{2+} Detection

As described above, TAS-COF exhibited favorable oxidase-like activity and could oxidize the colorless TMB into blue oxTMB. The oxTMB contained imines that could coordinate with UO_2^{2+} to produce a colorless complex [21]. Figure 3A illustrated the spectra of the TAS-COF + TMB system with the presence of UO_2^{2+} . A clear color change from blue to colorless was observed with the presence of UO_2^{2+} , providing the solid base for UO_2^{2+} detection.

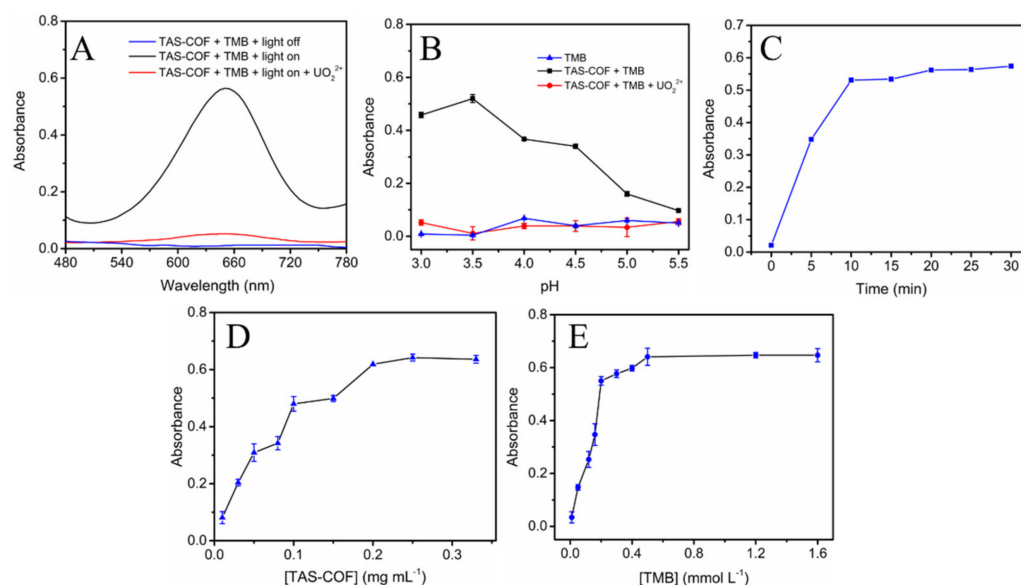


Figure 3. UV-vis spectra of TAS-COF + TMB system with/without the presence of UO_2^{2+} (A). The effect of pH on the absorbance at 650 nm of TMB, TAS-COF + TMB, TAS-COF + TMB + UO_2^{2+} under visible light irradiation (B). The effect of irradiation time (C), TAS-COF concentration (D), and TMB concentration (E) on the absorbance at 650 nm of the sensing system.

In order to achieve high sensitivity for the colorimetric monitoring of UO_2^{2+} based on the light-triggered oxidase-like activity of TAS-COF, the key detection parameters, including the reaction pH, irradiation time, TAS-COF dosage, and TMB concentration were optimized. It can be seen from Figure 3B that TAS-COF exhibited the best oxidase-like activity under pH 3.5, and the largest signal difference was achieved under the same pH condition. As shown in Figure 3C, the results indicate that the absorbance signal firstly increased obviously with the irradiation time, and then leveled off when the time was longer than 10 min. Meanwhile, it was found that the signal change increased with TAS-COF concentration up to 0.2 mg mL^{-1} , and the further increase in TAS-COF dosage made no contribution to the signal (Figure 3D). At the same time, a similar trend was observed for TMB concentration when the concentration increased to 0.5 mmol L^{-1} (Figure 3E), and the further increase in TMB concentration caused no obvious change in the absorbance signals due to the limited TAS-COF content. Therefore, the following optimal experimental

conditions were adopted for UO_2^{2+} detection: a TAS-COF concentration of 0.2 mg mL^{-1} , a TMB concentration of 0.5 mmol L^{-1} , a reaction pH of 3.5, and 10 min irradiation under a white-light LED lamp ($\lambda \geq 420 \text{ nm}$).

3.4. Analytical Performance for UO_2^{2+} Detection

The analytical performance for UO_2^{2+} detection was investigated by acquiring the absorbance signal after the addition of different concentrations of UO_2^{2+} under the optimal conditions. As depicted in Figure 4A, the absorbance of the TAS-COF + TMB sensing system changed obviously with UO_2^{2+} content. The absorbance signal difference ($A_0 - A$, A_0 and A represented the absorbance at 650 nm with/without the presence of UO_2^{2+}) showed a good linear relationship with UO_2^{2+} concentration in the range of $0.25\text{--}25 \text{ }\mu\text{mol L}^{-1}$ ($R^2 = 0.98$) (Figure 4B). The limit of detection (LOD, $3\sigma/k$) was deduced to be $0.07 \text{ }\mu\text{mol L}^{-1}$ ($27.6 \text{ }\mu\text{g}\cdot\text{L}^{-1}$), which was below the maximum pollution level of UO_2^{2+} in drinking water stipulated by the World Health Organization ($30 \text{ }\mu\text{g}\cdot\text{L}^{-1}$) [30]. Compared with the reported sensing system, the present colorimetric strategy also offered superior sensitivity toward UO_2^{2+} detection (Figure 4C) [31–37], contributed by the efficient light-triggered oxidase-like activity of TAS-COF.

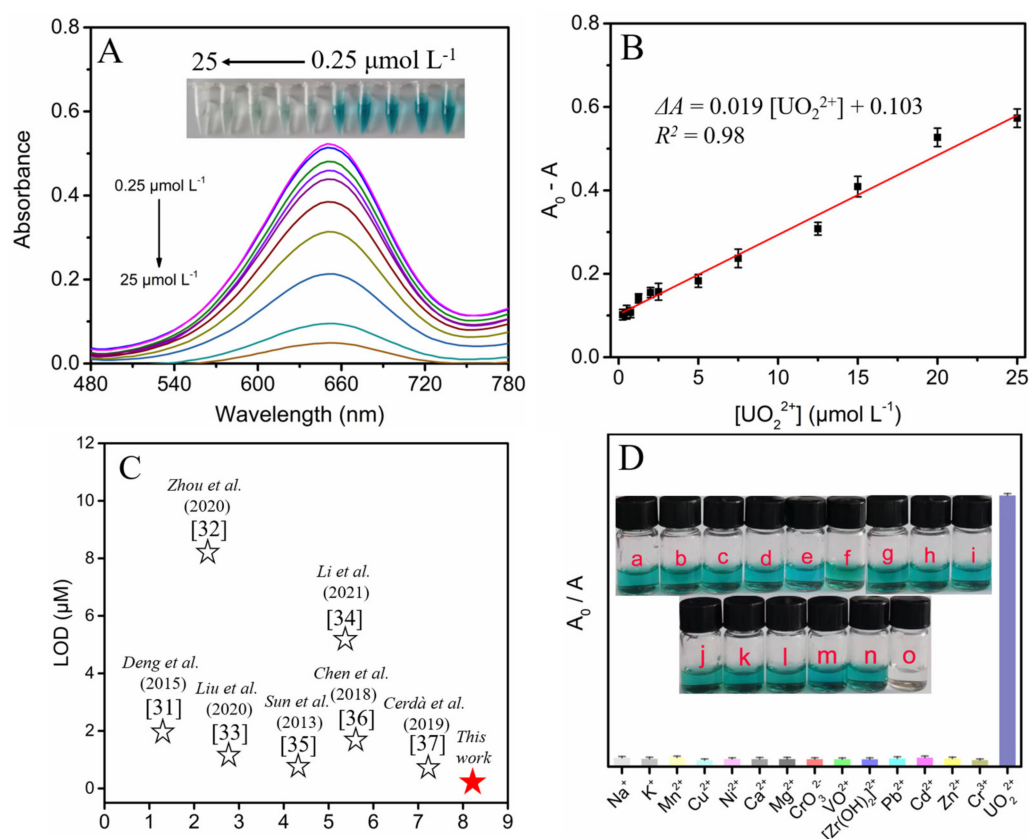


Figure 4. (A) UV-vis spectra of TAS-COF + TMB system with different UO_2^{2+} content under visible light irradiation. Inset: the images of the corresponding solutions. (B) The linear relationship between the absorbance ($A_0 - A$) and UO_2^{2+} concentration. (C) Comparison of the analytical performance for UO_2^{2+} assay (Refs. [31–37]). (D) Absorbance (A_0/A , in which A_0 and A represented the absorbance at 650 nm with/without the presence of UO_2^{2+}) intensity of the system after the addition of UO_2^{2+} and different cations. Insets show the images of the corresponding solutions. The error bars were estimated from triplicate measurements ($n = 3$).

The sensing selectivity is of particular significance in practical applications. The selectivity of this sensing system for UO_2^{2+} detection was then explored. The absorbance signals after the addition of a series of aqueous solutions containing potential interfering

ions of 5 equiv were recorded. As depicted in Figure 4D, negligible color change or absorbance variation was observed with the addition of interfering ions except for UO_2^{2+} . These suggested the favorable specificity of the present colorimetric sensing system for UO_2^{2+} determination.

3.5. Colorimetric Detection of UO_2^{2+} Content in Real Water Samples

To demonstrate the feasibility of the TAS-COF-based colorimetric procedure in UO_2^{2+} detection, UO_2^{2+} content in tap water (T) and lake water (L) samples were determined. To verify the accuracy of determination, UO_2^{2+} contents in these samples were also determined by ICP-MS.

As shown in Table 1, the recoveries ranged from 90.00% to 100.8% for the samples spiked with different levels of UO_2^{2+} , and the relative standard deviation (RSD) was less than 3.12%. Figure 5 also suggested that there was no significant difference in the found values of the samples among colorimetry modes. Moreover, the determination results agreed well with those from ICP-MS ($p > 0.05$), demonstrating that the TAS-COF-based colorimetric sensing platform was potentially sensitive and accurate in monitoring UO_2^{2+} content in complex matrix samples.

Table 1. The colorimetric analysis results for UO_2^{2+} in real samples.

Samples	Added (μM)	Found (μM)	Recovery (%)	ICP-MS	p Value (t -Test)
T-1#	0.5	0.48 ± 0.03	96.00 ± 1.02	0.49 ± 0.02	0.456
T-2#	5	5.04 ± 0.06	100.80 ± 1.51	5.01 ± 0.05	0.378
T-3#	10	9.95 ± 0.18	99.50 ± 0.42	9.99 ± 0.06	0.832
L-1#	0.5	0.45 ± 0.03	90.00 ± 0.87	0.51 ± 0.04	0.668
L-2#	5	4.97 ± 0.05	99.40 ± 3.12	4.95 ± 0.03	0.609
L-3#	10	10.06 ± 0.26	100.60 ± 1.03	10.01 ± 0.12	0.629

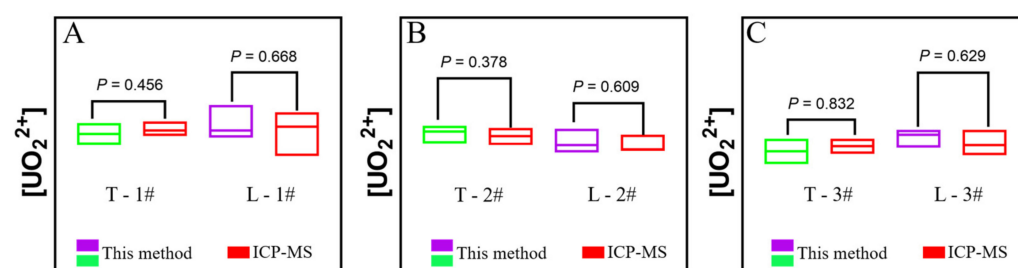


Figure 5. Floating bars plot of UO_2^{2+} contents of different samples by colorimetric assay. (A) T-1# and L-1#. (B) T-2# and L-2#. (C) T-3# and L-3#. (Student's t -test by GraphPad Prism 9, $p > 0.05$, no significant difference).

3.6. Visual Colorimetric Detection of UO_2^{2+}

The analytical performance of the paper-based visual colorimetric detection of UO_2^{2+} with TAS-COF was also inspected. The oxTMB product oxidized by TAS-COF presented a clear blue color in the absence of UO_2^{2+} and faded off gradually after the addition of UO_2^{2+} ranging from 0.5 mmol L^{-1} to 10 mmol L^{-1} (Figure 6). The color fading induced by the addition of UO_2^{2+} was readily observed by the naked eye. The visual detection of UO_2^{2+} contents in water samples was also performed. The color of the paper-based sensor after the addition of these spiked waters is similar to the UO_2^{2+} standard solution of UO_2^{2+} , suggesting that this paper-based sensor could provide a feasible visual detection platform for simple and rapid UO_2^{2+} content evaluation, which might provide a convenient tool for on-the-spot radionuclide detection.

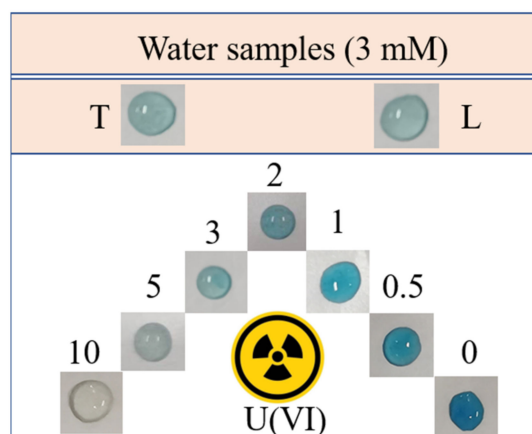


Figure 6. Photographs of the paper-based sensor under white-light LED lamp irradiation with the addition of different content of UO_2^{2+} . T: tap water, L: lake water.

4. Conclusions

In summary, we have developed a photosensitive sulfone-based COFs material via a Schiff base condensation reaction. The obtained TAS-COF showed oxidase-like activity under visible light irradiation and can direct catalysis of colorless TMB into blue product oxTMB. The presence of UO_2^{2+} will induce clear color fading of this system due to the coordination between oxTMB and UO_2^{2+} . A sensitive colorimetric strategy was thus built for the monitoring of UO_2^{2+} content. Meanwhile, the detection of UO_2^{2+} content on a paper-based sensor via visual inspection mode is also achieved, providing a powerful tool for the simple on-the-spot colorimetric UO_2^{2+} analysis in real water samples. This research not only provides a potential path for radionuclide quantitative assay but also expands the applications of COF in sensing by taking advantage of its unique structure and favorable photosensitive properties.

Author Contributions: Conceptualization, methodology, validation, formal analysis, investigation, data curation, writing—original draft preparation, Y.X.; conceptualization, J.W.; supervision, project administration, funding acquisition, writing—review and editing, X.C.; All authors have read and agreed to the published version of the manuscript.

Funding: This research was funded by Liaoning Science and Technology Development Foundation Guided by Central Government (2022JH6/100100024) and Fundamental Research Funds for the Central Universities, China (N2005027).

Institutional Review Board Statement: Not applicable.

Informed Consent Statement: Not applicable.

Data Availability Statement: Not applicable.

Conflicts of Interest: The authors declare no conflict of interest.

References

- Chen, M.; Liu, T.; Zhang, X.; Zhang, R.; Tang, S.; Yuan, Y.; Xie, Z.; Liu, Y.; Wang, H.; Fedorovich, K.; et al. Photoinduced enhancement of uranium extraction from seawater by MOF/black phosphorus quantum dots heterojunction anchored on cellulose nanofiber aerogel. *Adv. Funct. Mater.* **2021**, *31*, 2100106. [[CrossRef](#)]
- Veiga, H.; Amaral, C.; Fernandes, M. Human health risk screening of radioactive and nonradioactive contaminants due to uranium industry operation. *J. Environ. Radioact.* **1998**, *39*, 69–85. [[CrossRef](#)]
- Silva, R.; Kazimi, M.; Hejzlar, P. Nuclear fuel recycling: National and regional options for the US nuclear energy system. *Energy Environ. Sci.* **2010**, *3*, 996. [[CrossRef](#)]
- Chen, X.; Zheng, W.; Anbar, A. Uranium Isotope fractionation ($(^{238}\text{U})/(^{235}\text{U})$) during U(VI) uptake by freshwater plankton. *Environ. Sci. Technol.* **2020**, *54*, 2744–2752. [[CrossRef](#)] [[PubMed](#)]
- Moshe, M.; Elbaz, J.; Willner, I. Sensing of UO_2^{2+} and design of logic gates by the application of supramolecular constructs of ion-dependent DNAzymes. *Nano Lett.* **2009**, *9*, 1196–1200. [[CrossRef](#)] [[PubMed](#)]

6. Lorber, A.; Karpas, Z.; Halicz, L. Flow injection method for determination of uranium in urine and serum by inductively coupled plasma mass spectrometry. *Anal. Chim. Acta* **1996**, *334*, 295–301. [[CrossRef](#)]
7. Ruan, C.; Luo, W.; Wang, W.; Gu, B. Surface-enhanced Raman spectroscopy for uranium detection and analysis in environmental samples. *Anal. Chim. Acta* **2007**, *605*, 80–86. [[CrossRef](#)]
8. Abbasi, S. Atomic absorption spectrometric and spectrophotometric trace analysis of uranium in environmental samples with n-p-methoxyphenyl-2-furylacryloylhydroxamic acid and 4-(2-pyridylazo) resorcinol. *Int. J. Environ. Anal. Chem.* **2006**, *36*, 163–172. [[CrossRef](#)]
9. Lee, J.; Wang, Z.; Liu, J.; Lu, Y. Highly sensitive and selective colorimetric sensors for uranyl (UO_2^{2+}): Development and comparison of labeled and label-free DNAzyme-gold nanoparticle systems. *J. Am. Chem. Soc.* **2008**, *130*, 14217–14226. [[CrossRef](#)]
10. Cao, X.; Zhang, H.; Ma, R.; Yang, Q.; Zhang, Z.; Liu, Y. Visual colorimetric detection of UO_2^{2+} using o-phosphorylethanolamine-functionalized gold nanoparticles. *Sens. Actuators B Chem.* **2015**, *218*, 67–72. [[CrossRef](#)]
11. Jiang, Z.; Li, H.; Ai, R.; Deng, Y.; He, Y. Electrostatic-driven coordination interaction enables high specificity of UO_2^{2+} peroxidase mimic for visual colorimetric detection of UO_2^{2+} . *ACS Sustain. Chem. Eng.* **2020**, *8*, 11630–11637. [[CrossRef](#)]
12. Li, S.; Zhao, X.; Gang, R.; Cao, B.; Wang, H. Doping nitrogen into Q-graphene by plasma treatment toward peroxidase mimics with enhanced catalysis. *Anal. Chem.* **2020**, *92*, 5152–5157. [[CrossRef](#)]
13. Ding, Y.; Ren, G.; Wang, G.; Lu, M.; Liu, J.; Li, K.; Lin, Y. V_2O_5 nanobelts mimic tandem enzymes to achieve nonenzymatic online monitoring of glucose in living rat brain. *Anal. Chem.* **2020**, *92*, 4583–4591. [[CrossRef](#)]
14. Liu, Z.; Wang, F.; Ren, J.; Qu, X. A series of MOF/Ce-based nanozymes with dual enzyme-like activity disrupting biofilms and hindering recolonization of bacteria. *Biomaterials* **2019**, *208*, 21–31. [[CrossRef](#)]
15. Deng, H.; Lin, X.; Liu, Y.; Li, K.; Zhuang, Q.; Peng, H.; Liu, A.; Xia, X.; Chen, W. Chitosan-stabilized platinum nanoparticles as effective oxidase mimics for colorimetric detection of acid phosphatase. *Nanoscale* **2017**, *9*, 10292–10300. [[CrossRef](#)]
16. He, W.; Liu, Y.; Yuan, J.; Yin, J.; Wu, X.; Hu, X.; Zhang, K.; Liu, J.; Chen, C.; Ji, Y.; et al. Au@Pt nanostructures as oxidase and peroxidase mimetics for use in immunoassays. *Biomaterials* **2011**, *32*, 1139–1147. [[CrossRef](#)]
17. Guo, Y.; Tao, Y.; Ma, X.; Jin, J.; Wen, S.; Ji, W.; Song, W.; Zhao, B.; Ozaki, Y. A dual colorimetric and SERS detection of Hg^{2+} based on the stimulus of intrinsic oxidase-like catalytic activity of Ag-CoFe₂O₄/reduced graphene oxide nanocomposites. *Chem. Eng. J.* **2018**, *350*, 120–130. [[CrossRef](#)]
18. Sang, Y.; Li, W.; Liu, H.; Zhang, L.; Wang, H.; Liu, Z.; Ren, J.; Qu, X. Construction of nanozyme-hydrogel for enhanced capture and elimination of bacteria. *Adv. Funct. Mater.* **2019**, *29*, 1900518. [[CrossRef](#)]
19. Sun, A.; Mu, L.; Hu, X. Graphene oxide quantum dots as novel nanozymes for alcohol intoxication. *ACS Appl. Mater. Interfaces* **2017**, *9*, 12241–12252. [[CrossRef](#)]
20. Pachful, P.; Acharjya, A.; Roeser, J.; Sivasankaran, R.; Ye, M.; Brückner, A.; Schmidt, J.; Thomas, A. Donor-acceptor covalent organic frameworks for visible light induced free radical polymerization. *Chem. Mater.* **2019**, *10*, 8316–8322. [[CrossRef](#)]
21. Zhang, L.; Yang, G.; Xiao, S.; Tan, Q.; Zheng, Q.; Liang, R.; Qiu, J. Facile construction of covalent organic framework nanozyme for colorimetric detection of uranium. *Small* **2021**, *17*, 2102944. [[CrossRef](#)]
22. Jin, P.; Niu, X.; Zhang, F.; Dong, K.; Dai, H.; Zhang, H.; Wang, W.; Chen, H.; Chen, X. Stable and reusable light-responsive reduced covalent organic framework (COF-300-AR) as an oxidase-mimicking catalyst for GSH detection in cell lysate. *ACS Appl. Mater. Interfaces* **2020**, *12*, 20414–20422. [[CrossRef](#)]
23. Faure, M.; Sotta, B.; Gamby, J. Investigating the kinetics of paramagnetic-beads linked alkaline phosphatase enzyme through microchannel resistance measurement in dielectric microchip. *Biosens. Bioelectron.* **2014**, *58*, 61–67. [[CrossRef](#)]
24. Mitra, S.; Kandambeth, S.; Biswal, B.; Khayum, A.; Choudhury, C.; Mehta, M.; Kaur, G.; Banerjee, S.; Prabhune, A.; Verma, S.; et al. Self-exfoliated guanidinium-based ionic covalent organic nanosheets (iCONs). *J. Am. Chem. Soc.* **2016**, *8*, 2823–2828. [[CrossRef](#)]
25. Zhi, Y.; Li, Z.; Feng, X.; Xia, H.; Zhang, Y.; Shi, Z.; Mu, Y.; Liu, X. Covalent organic frameworks as metal-free heterogeneous photocatalysts for organic transformations. *J. Mater. Chem. A* **2017**, *5*, 22933–22938. [[CrossRef](#)]
26. Zhang, Y.; Song, J.; Shao, W.; Li, J. Au@NH₂-MIL-125(Ti) heterostructure as light-responsive oxidase-like mimic for colorimetric sensing of cysteine. *Microporous Mesoporous Mater.* **2021**, *310*, 110642. [[CrossRef](#)]
27. Wang, S.; Wang, M.; Liu, Y.; Meng, X.; Ye, Y.; Song, X.; Liang, Z. Novel D- π -A conjugated microporous polymer as visible light-driven oxidase mimic for efficient colorimetric detection of glutathione. *Sens. Actuators B Chem.* **2021**, *326*, 128808. [[CrossRef](#)]
28. Kari, J.; Andersen, M.; Borch, K.; Westh, P. An inverse Michaelis-Menten approach for interfacial enzyme kinetics. *ACS Catal.* **2017**, *7*, 4904–4914. [[CrossRef](#)]
29. Gao, L.; Zhuang, J.; Nie, L.; Zhang, J.; Zhang, Y.; Gu, N.; Wang, T.; Feng, J.; Yang, D.; Perrett, S.; et al. Intrinsic peroxidase-like activity of ferromagnetic nanoparticles. *Nat. Nanotechnol.* **2007**, *2*, 577–583. [[CrossRef](#)]
30. Deng, X.; Fang, Y.; Lin, S.; Cheng, Q.; Liu, Q.; Zhang, X. Porphyrin-based porous organic frameworks as a biomimetic catalyst for highly efficient colorimetric immunoassay. *ACS Appl. Mater. Interfaces* **2017**, *9*, 3514–3523. [[CrossRef](#)]
31. Zhang, D.; Chen, Z.; Omar, H.; Deng, L.; Khashab, N. Colorimetric peroxidase mimetic assay for uranyl detection in seawater. *ACS Appl. Mater. Interfaces* **2015**, *7*, 4589–4594. [[CrossRef](#)] [[PubMed](#)]
32. Qian, J.; Cao, N.; Zhang, J.; Hou, J.; Chen, Q.; Zhang, C.; Sun, Y.; Liu, S.; He, L.; Zhang, K.; et al. Field-portable ratiometric fluorescence imaging of dual-color label-free carbon dots for uranyl ions detection with cellphone-based optical platform. *Chin. Chem. Lett.* **2020**, *31*, 2925–2928. [[CrossRef](#)]

33. Guo, W.; Xu, H.; Cao, X.; Ma, J.; Liu, Y. A novel electrochemical determination platform of uranyl ion based on silver nanodendrites-reduced graphene oxide. *Microchem. J.* **2020**, *158*, 105134. [[CrossRef](#)]
34. Chen, L.; Liu, J.; Cao, C.; Tang, S.; Lv, C.; Xiao, X.; Yang, S.; Liu, L.; Sun, L.; Zhu, B.; et al. Dual-signal amplification electrochemical sensing for the sensitive detection of uranyl ion based on gold nanoparticles and hybridization chain reaction-assisted synthesis of silver nanoclusters. *Anal. Chim. Acta* **2021**, *1*, 338986. [[CrossRef](#)]
35. Yang, W.; Bai, Z.; Shi, W.; Yuan, L.; Tian, T.; Chai, Z.; Wang, H.; Sun, Z. MOF-76: From a luminescent probe to highly efficient U(VI) sorption material. *Chem. Commun. (Camb)* **2013**, *49*, 10415–10417. [[CrossRef](#)]
36. Wang, Z.; Xu, C.; Lu, Y.; Wei, G.; Ye, G.; Sun, T.; Chen, J. Microplasma electrochemistry controlled rapid preparation of fluorescent polydopamine nanoparticles and their application in uranium detection. *Chem. Eng. J.* **2018**, *344*, 480–486. [[CrossRef](#)]
37. Danchana, K.; Souza, C.; Palacio, E.; Cerdà, V. Multisyringe flow injection analysis for the spectrophotometric determination of uranium (VI) with 2-(5-bromo-2-pyridylazo)-5-diethylaminophenol. *Microchem. J.* **2019**, *150*, 104148. [[CrossRef](#)]